

Unraveling the effect of local dopant environment on NiO₆ octahedron perturbation for enhanced oxygen evolution activity

Junchen Yu ^{a,1}, Haoyin Zhong ^{a,1}, Qi Zhang ^{a,1}, Chao Wu ^{b,d}, Xin Zhang ^a, Shanlin Li ^a, Yongzhi Zhao ^a, Hang An ^a, Yifan Ma ^a, Zhigen Yu ^c, Shibo Xi ^{d,*}, Xiaopeng Wang ^{a,b,**}, Junmin Xue ^{a,*2}

^a Department of Materials Science and Engineering, National University of Singapore, Singapore 117575, Singapore

^b College of Materials Science and Engineering, Sichuan University, Chengdu 610065, China

^c Institute of High Performance Computing, Agency for Science, Technology and Research, Singapore 138632, Singapore

^d Institute of Sustainability for Chemicals, Energy, and Environment (ISCE2), Singapore 627833, Singapore



ARTICLE INFO

Keywords:

Oxygen evolution reaction
NiO₆ octahedron distortion
 e_g^* band broadening
Local dopant environment
Electron transfer

ABSTRACT

The oxygen evolution reaction (OER) performance in cation-doped materials often exhibits a volcano-like relationship with dopant concentration. However, the influence of dopant content with its associated local environment on the electronic states of electrocatalysts remains unclear. Herein, V is incorporated into Ni(OH)₂ to study the underlying mechanism. It is revealed that evenly distributed V can effectively perturb the NiO₆ octahedron, leading to strong e_g^* band broadening and more electronic states around the Fermi level. This phenomenon significantly enhances the electron transfer from electrocatalysts to external circuits. Conversely, the aggregation of V at higher dopant concentration exerts weaker influence on perturbing the NiO₆ octahedron. As a result of balance between V doping and aggregation, Ni_{0.95}V_{0.05}OOH, with the strongest NiO₆ octahedron distortion, effectuating a remarkably low overpotential of 258 mV at 10 mA cm⁻². Furthermore, such a structure-activity relationship is also extended to Fe-doped Ni(OH)₂, affirming the universality of the proposed mechanism.

1. Introduction

Sustainable energy derived from natural sources, such as solar, wind, and tidal power, offers a promising avenue for shaping a resilient future. This entails reducing our dependence on traditional fossil fuels and mitigating the impact of greenhouse gas emissions [1–3]. However, the intermittent nature of these renewable energy sources, which closely align with seasonal and weather patterns, severely curtails their widespread deployment [4–6]. In this context, electrochemical water splitting emerges as a potent technique for storing surplus intermittent energy-generated electricity by producing hydrogen gas as a sustainable and clean energy carrier [7]. Yet, the efficiency of water splitting is significantly constrained by the sluggishness of the oxygen evolution reaction (OER), which involves four-electron transfer steps [8,9]. Consequently, extensive research efforts have been directed towards

developing durable and earth-abundant OER electrocatalysts with satisfactory performance, particularly compounds based on first-row transition metals i.e. Mn, Fe, Co, Ni, etc [10–13].

To date, it is well-established that under alkaline anodic conditions, most transition metal-based compounds would undergo surface reconstruction, forming transition metal-based oxyhydroxides (MOOH) as the real catalytic species [14–16]. However, pristine MOOH typically exhibits limited intrinsic catalytic activity [17,18]. As a result, considerable research efforts have been devoted to enhancing the OER performance of MOOH, such as morphology engineering [19,20], anion regulation [21–23], cation doping [24,25] and interface engineering [26,27]. Recently, the concept of symmetry breaking in oxygen octahedron and subsequent lattice distortion in oxides has been demonstrated as a central issue in oxide-based electrocatalysts for improved OER activity [28–33]. Our prior research revealed the pivotal role of

* Corresponding authors.

** Corresponding author at: Department of Materials Science and Engineering, National University of Singapore, Singapore 117575, Singapore.

E-mail addresses: xi_shibo@ices.a-star.edu.sg (S. Xi), msewxia@nus.edu.sg (X. Wang), msexuejm@nus.edu.sg (J. Xue).

¹ These authors contributed equally.

² Lead contact

NiO_6 octahedron distortion in tuning the e_g^* band broadening in NiOOH -based materials [17]. Specifically, it was revealed that doping certain amount of Fe could effectively induce the NiO_6 octahedron perturbation. A stronger degree of NiO_6 octahedron distortion would lead to higher extent of e_g^* band broadening, which is essential to facilitate the electron transfer from electrocatalysts to the external circuit. Despite understanding the importance of oxygen octahedron perturbation in optimizing catalytic activity, the OER performance also shows a strong dependence on dopant concentration, often exhibiting a volcano-like correlation between dopant proportion and OER activity [13,34]. As such, it is of great importance to understand the influence of dopant content and its corresponding local environment on the oxygen octahedron distortion of electrocatalysts, which is still not well experimentally accounted for.

To explore the underlying mechanism, $\text{Ni}_{1-x}\text{V}_x(\text{OH})_2$ ($x = 0.02, 0.05, 0.1$) are prepared as model materials. The OER inactive V is a suitable element to study the doping effect on the electronic states and corresponding OER activity of electrocatalysts [35–39]. Detailed X-ray adsorption fine-structure spectroscopy (XAFS) analysis reveals a volcano-like relationship between the V dopant content and the extent of NiO_6 octahedron perturbation, with the strongest NiO_6 distortion observed at $\sim 5\%$ V content. Theoretical analysis of V-O bond length together with V K-edge Fourier transformed extended X-ray near fine structure (FT-EXAFS) spectra show that the local environment of V becomes increasingly irregular as V content increases. These findings suggest that V dopants at higher concentration would tend to aggregate in the lattice, resulting in weaker effects on perturbing the NiO_6 octahedron in $\text{Ni}(\text{OH})_2$. Further theoretical calculation indicates that the uniformly distributed V could effectively perturb the NiO_6 octahedron, leading to strong e_g^* band broadening. This phenomenon could significantly increase the number of electronic states around the Fermi level, thereby facilitating electron transfer from electrocatalysts to the external circuit. Conversely, the aggregation of V shows a weaker impact on tuning the NiO_6 octahedron distortion and results in fewer electronic states around the Fermi level. As a result of balance between V doping and V aggregation, $\text{Ni}_{0.95}\text{V}_{0.05}\text{OOH}$, with the strongest NiO_6 octahedron distortion, delivers the best OER performance among all the studied samples, effectuating a remarkably low overpotential of 258 mV at 10 mA cm⁻². Furthermore, the universality of the proposed understanding on the influence of local dopant environment on the oxygen octahedron perturbation and corresponding OER activity is successfully extended to the widely studied Fe-doped $\text{Ni}(\text{OH})_2$ system. It is highly expected that these findings will help better understand other cation-doped materials and offer guidelines for designing systems with excellent OER activity.

2. Experimental section

2.1. Materials

Nickel nitrate hexahydrate ($\text{Ni}(\text{NO}_3)_2 \bullet 6 \text{ H}_2\text{O}$, $\geq 98.0\%$), Vanadium chloride (VCl_3 , 97.0%), Iron nitrate nonahydrate ($\text{Fe}(\text{NO}_3)_3 \bullet 9 \text{ H}_2\text{O}$, $\geq 98.0\%$) and Urea ($\text{CH}_4\text{N}_2\text{O}$, 99%~100.5%) were purchased from the Sigma-Aldrich. Carbon cloth (W0S1011) was obtained from CeTech. Deionized (DI) water was produced by a Milipore TankPE30 water purification machine. All chemicals were reagent grade and used without further purification.

2.2. Synthesis of the $\text{Ni}_{1-x}\text{V}_x(\text{OH})_2$ ($x = 0, 0.02, 0.05, 0.1$) and $\text{Ni}_{1-x}\text{Fe}_x(\text{OH})_2$ ($x = 0.05, 0.20, 0.40, 0.60, 0.80$) on carbon cloth (CC)

CC was heat-treated at 500 °C for 1 h in air to increase its wettability and dealt with Ultra-Violet Ozone for 30 min to make it fully hydrophilic. The CC was then cleaned several times with DI water. Next, different mole ratios of Ni/V solutions (1:0, 98:2, 95:5, 9:1, for the synthesis of pure $\text{Ni}(\text{OH})_2$, $\text{Ni}_{0.98}\text{V}_{0.02}(\text{OH})_2$, $\text{Ni}_{0.95}\text{V}_{0.05}(\text{OH})_2$, $\text{Ni}_{0.9}\text{V}_{0.1}(\text{OH})_2$, respectively) were obtained by mixing $\text{Ni}(\text{NO}_3)_2 \bullet 6 \text{ H}_2\text{O}$

and VCl_3 in 35 mL H_2O , while the total amount of metal ions ($\text{Ni}^{2+} + \text{V}^{3+}$) was kept to 2 mmol. Afterwards, 0.3 g of urea was added to the solution and a cleaned 2 cm × 1.5 cm CC was immersed in it. The aqueous solutions and CC were transferred into a Teflon-lined stainless-steel autoclave and the system was maintained at 120 °C for 10 h. Finally, the prepared samples were washed with DI water, and dried at 60 °C for 6 h in oven. The $\text{Ni}_{1-x}\text{Fe}_x(\text{OH})_2$ ($x = 0.05, 0.20, 0.40, 0.60, 0.80$) were fabricated on CC by hydrothermal method [17].

2.3. Removal of Fe impurity

The 1 M KOH solution was purified to remove Fe impurity before use as the electrolyte. The procedure was as follows: First, 0.5 g $\text{Ni}(\text{NO}_3)_2 \bullet 6 \text{ H}_2\text{O}$ powder was added into 30 mL 1 M KOH solution, forming $\text{Ni}(\text{OH})_2$ precipitation. Next, the suspension was centrifuged at 10,000 r/min for 3 times. The centrifugation process was repeated for 3 times. Then, the obtained $\text{Ni}(\text{OH})_2$ powder was added into 50 mL KOH solution and mechanically agitated for 10 min. After standing still for 24 h, the suspension was centrifuged with the KOH supernatant decanted into a clean electrochemical cell for use.

2.4. Material characterizations

X-ray diffraction (XRD) measurements were performed on a Bruker D8 Advance X-ray diffractometer with Cu K α radiation ($\lambda = 1.5406 \text{ \AA}$). The scanning electron microscopy (SEM) was conducted on a ZEISS G300. The transmission electron microscopy (TEM) combined with energy dispersive X-ray spectroscopy (EDS) was conducted on a JEOL 2100 F. Inductively coupled plasma (ICP) mass spectrometry was measured on an Agilent ICP-OES730. The Nickel and Vanadium K-edge X-ray absorption fine structure (XAFS) spectra were recorded at the XAFCA beamline at the Singapore Synchrotron Light Source (SSLS) center under transmission mode, the storage ring ran at 0.7 GeV with an average electron current below 250 mA. The energy calibrations were finished by using standard Nickel foil and Vanadium foil. The k^2 -weighted Fourier transforms were performed using the Hanning window function for the EXAFS results with the k-range of 2.3–12.7 Å⁻¹ for Ni and 2.2–10.5 Å⁻¹ for V. The X-ray photoelectron spectroscopy (XPS) was measured by a Thermo Fisher Scientific ESCALAB 250i spectrometer equipped with Al K α X-ray irradiation source (1486.68 eV).

2.5. Electrochemical measurements

Electrochemical measurements were performed using a three-electrode system, with the as prepared sample as the working electrode, Hg/HgO as the reference electrode, and Pt as the counter electrode. All the reference electrodes used in this experiment are calibrated vs. reversible hydrogen electrode (RHE). The electrochemical workstation used for these electrochemical measurements was VMP3 (BioLogic Inc), with built-in electrochemical impedance spectroscopy (EIS) analyzer. The EIS spectra were conducted at 0 V (vs. open circuit voltage), and the frequency ranged from 100 kHz to 100 Hz. The linear scan voltammetry (LSV) was measured at scan rate 0.1 mV s⁻¹. The Tafel plots were derived by plotting the overpotential η (mV) versus the log current density($\log[J]$). The Tafel slope was obtained via linearly fitting the linear portion of the Tafel plots according to the Tafel equation ($\eta = b \log[J] + a$, b is the Tafel slope). The electrochemical active surface area (ECSA) data was evaluated from recording the electrochemical double-layer capacitance of the catalyst via cyclic voltammograms (CVs). Here, the potential range was set at 0.02–0.12 V (versus Hg/HgO) to avoid the Faradaic process. The CVs were conducted in the quiescent electrolyte with the potential swept across the set potential range with at 6 scan rates including 5, 10, 20, 30, 40, 50 mV s⁻¹. The charging current was plotted versus scan rate and a straight line could be derived with the slope value equaled to the double-layer capacitance (C_{dl}). The ECSA was obtained by dividing the C_{dl} to the specific capacitance $C_s = 0.04 \text{ mF}$

cm^{-2} . For the pulse-voltammetry test, a $0.2 \text{ cm} \times 0.5 \text{ cm}$ carbon cloth grown with electrocatalysts was used. The potential was set firstly at a low potential (E_{low}) for 6 s, then turned to a higher potential (E_{high}) for 6 s before back to E_{low} for 6 s. This cycle was repeated while increasing E_{high} from 1.42 V to 1.68 V versus RHE in 20 mV/step with constant $E_{\text{low}} = 1.4 \text{ V}$. The transferred charge normalized to ECSA during each cycle was evaluated by integrating the current pulse/ECSA over time.

2.6. Computational details

All density functional theory (DFT) calculations were performed by the Vienna Ab initio Simulation Package (VASP) combined with Perdew–Burke–Ernzerhof (PBE) functional [40] and DFT+U (U-J=5.3 for Ni and 3.4 for V, respectively) [41]. Projector augmented-wave (PAW) pseudopotentials [42] and DFT-D3 dispersion correction [43] were used in all calculations. The plane wave kinetic energy cutoff was set to 500 eV and the energy and force convergence criteria were set to 10^{-5} eV and $0.02 \text{ eV } \text{\AA}^{-1}$, respectively. Densities of states (DOS) were calculated by VASPKIT [44] and the structures were visualized by VESTA [45].

The band center was calculated by

$$\text{band center} = \frac{\int n(\epsilon) \epsilon d\epsilon}{\int n(\epsilon) d\epsilon}$$

The OER overpotential step diagram was calculated by the classic AEM mechanism, and the thermal correction to Gibbs Free Energy of each state was calculated by VASPKIT. The free energy change of each

step was calculated by

$$\Delta G(1) = G(*\text{O}) + \frac{G(\text{H}_2)}{2} - G(*\text{OH})$$

$$\Delta G(2) = G(*\text{OOH}) + \frac{G(\text{H}_2)}{2} - G(*\text{O}) - G(\text{H}_2\text{O})$$

$$\Delta G(3) = G(*) + G(\text{O}_2) + \frac{G(\text{H}_2)}{2} - G(*\text{OOH})$$

$$\Delta G(4) = G(*\text{OH}) + \frac{G(\text{H}_2)}{2} - G(*) - G(\text{H}_2\text{O})$$

3. Results and discussion

3.1. Characterization of NiO_6 octahedron distortion in $\text{Ni}_{1-x}\text{V}_x(\text{OH})_2$ ($x = 0, 0.02, 0.05, 0.10$)

Herein, the $\text{Ni}_{1-x}\text{V}_x(\text{OH})_2$ ($x = 0.02, 0.05, 0.1$) samples are prepared via hydrothermal method (Detailed procedures are provided in experimental section). X-ray diffraction (XRD) pattern shows that all of these samples have similar diffraction peaks belonging to the $\text{Ni}(\text{OH})_2$ (JCPDS No. 38-0715), indicating the V cations have been successfully doped into the $\text{Ni}(\text{OH})_2$ lattice. (Fig. 1a) Transmission electron microscopy (TEM) images display nanosheet morphology for $\text{Ni}_{1-x}\text{V}_x(\text{OH})_2$ ($x = 0.02, 0.05, 0.1$) with no discernible differences in particle size (Fig. S1). Both scanning electron microscopy - energy dispersive x-ray

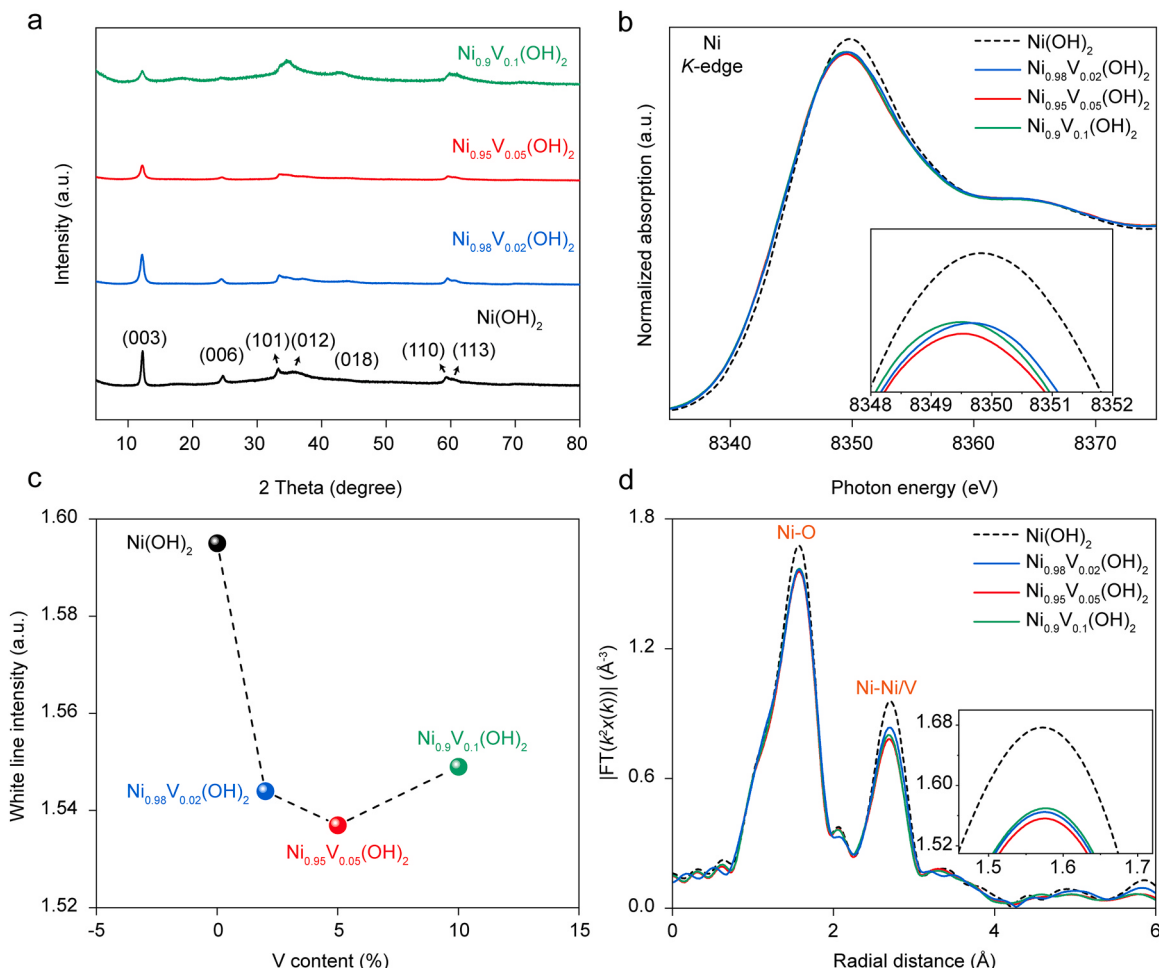


Fig. 1. Structural characterization of $\text{Ni}_{1-x}\text{V}_x(\text{OH})_2$ ($x = 0, 0.02, 0.05, 0.10$). a, XRD patterns of as-synthesized $\text{Ni}_{1-x}\text{V}_x(\text{OH})_2$ ($x = 0, 0.02, 0.05, 0.10$). b, Normalized Ni K-edge spectra of $\text{Ni}_{1-x}\text{V}_x(\text{OH})_2$ ($x = 0, 0.02, 0.05, 0.10$). c, Correlation between Ni K-edge white line intensity and V dopants content in $\text{Ni}_{1-x}\text{V}_x(\text{OH})_2$. d, FT-EXAFS spectra of $\text{Ni}_{1-x}\text{V}_x(\text{OH})_2$ ($x = 0, 0.02, 0.05, 0.10$).

spectroscopy (SEM-EDS) and transmission electron microscopy - energy dispersive x-ray spectroscopy (TEM-EDS) images confirm the uniform distribution of Ni, V and O elements in $\text{Ni}_{1-x}\text{V}_x(\text{OH})_2$ ($x = 0, 0.02, 0.05, 0.10$) over a large scale (Figs. S2-S6). The molar ratio of Ni to V is determined to be 49.81: 0.81 for $\text{Ni}_{0.98}\text{V}_{0.02}(\text{OH})_2$, 49.14: 2.28 for $\text{Ni}_{0.95}\text{V}_{0.05}(\text{OH})_2$, and 48.46: 4.54 for $\text{Ni}_{0.9}\text{V}_{0.1}(\text{OH})_2$, respectively, using inductive coupled plasma (ICP). These ratios are consistent with the calculated ratios (Table S1).

Next, the influence of V dopant on the structural characteristics of $\text{Ni}(\text{OH})_2$ is carefully evaluated via XAFS, with hydrothermal prepared $\text{Ni}(\text{OH})_2$ as the benchmark sample. As shown in Fig. 1b, the Ni K-edge XAFS spectra of these samples exhibit remarkably similar profiles compared to the benchmark $\text{Ni}(\text{OH})_2$. This similarity suggests that nearly all the Ni atoms in $\text{Ni}_{1-x}\text{V}_x(\text{OH})_2$ follow the NiO_6 octahedral geometry [15,17]. Moreover, both the energy of the white line peak and the photon energy positions at absorption ~ 0.5 of all V-doped $\text{Ni}(\text{OH})_2$ samples shift to lower energy among introducing V into $\text{Ni}(\text{OH})_2$. (Fig. 1b and Fig. S7) These results indicate that V cations are incorporated into the $\text{Ni}(\text{OH})_2$ lattice, which leads to slightly decreased valence state of Ni. Thus, the incorporation of V up to 10% would not break the octahedral structure of NiO_6 in $\text{Ni}(\text{OH})_2$. With this regard, the NiO_6 octahedron perturbation could be analyzed by observing the white line in Ni K-edge spectra, as a broader white line with lower intensity usually reflects a stronger extent of NiO_6 octahedron distortion in $\text{Ni}(\text{OH})_2$ configuration [17]. Specifically, with the white line intensity derived from Fig. 1b, Fig. 1c demonstrates the correlation between V dopant content and the extent of NiO_6 octahedron distortion in $\text{Ni}_{1-x}\text{V}_x(\text{OH})_2$ ($x = 0, 0.02, 0.05, 0.1$). Notably, the white line intensity of $\text{Ni}_{0.98}\text{V}_{0.02}(\text{OH})_2$ is significantly lower than that of the benchmark Ni

$(\text{OH})_2$, indicating that only $\sim 2\%$ of V dopant in $\text{Ni}(\text{OH})_2$ would be able to induce strong NiO_6 perturbation. When the V dopant content reaches 5%, the white line intensity decreases even further. Nonetheless, it is noteworthy that the white line intensity in $\text{Ni}_{0.9}\text{V}_{0.1}(\text{OH})_2$ surpasses that of $\text{Ni}_{0.98}\text{V}_{0.02}(\text{OH})_2$ and $\text{Ni}_{0.95}\text{V}_{0.05}(\text{OH})_2$. This result implies that further increasing the V dopant concentration diminishes the perturbation effect on the NiO_6 octahedral configuration. The effect of V dopant on perturbing the NiO_6 octahedron could also be examined through FT-EXAFS spectra, as a lower Ni-O bond peak intensity would indicate a locally more distorted structure [17]. As depicted in Fig. 1d, the intensity of the Ni-O bond peak ($\sim 1.56 \text{ \AA}$) gradually decreases with increasing V dopant content. However, this trend reverses when the V dopant content reaches $\sim 10\%$. Consequently, the degree of the Ni-O local structural distortion within $\text{Ni}_{1-x}\text{V}_x(\text{OH})_2$ ($x = 0, 0.02, 0.05, 0.1$) shows a discernible trend resembling a volcano curve in relation to the V dopant content. This phenomenon aligns harmoniously with the results derived from the Ni K-edge XAFS spectra.

3.2. Effects of local V dopants environment on the NiO_6 octahedron distortion

To explore the structural origin of the identified volcano-like relationship between the V dopant concentration and the degree of NiO_6 octahedron distortion, it is highly necessary to firstly investigate the local environment of V dopant in the host lattice. Hence, the V K-edge XAFS spectra are measured to study the geometry structures of V dopants at different portions. As shown in Fig. 2a, the rising edge of V K-edge spectra become lower and broader as V dopants content increases, indicating that the V-O local environment turns to be more disordered.

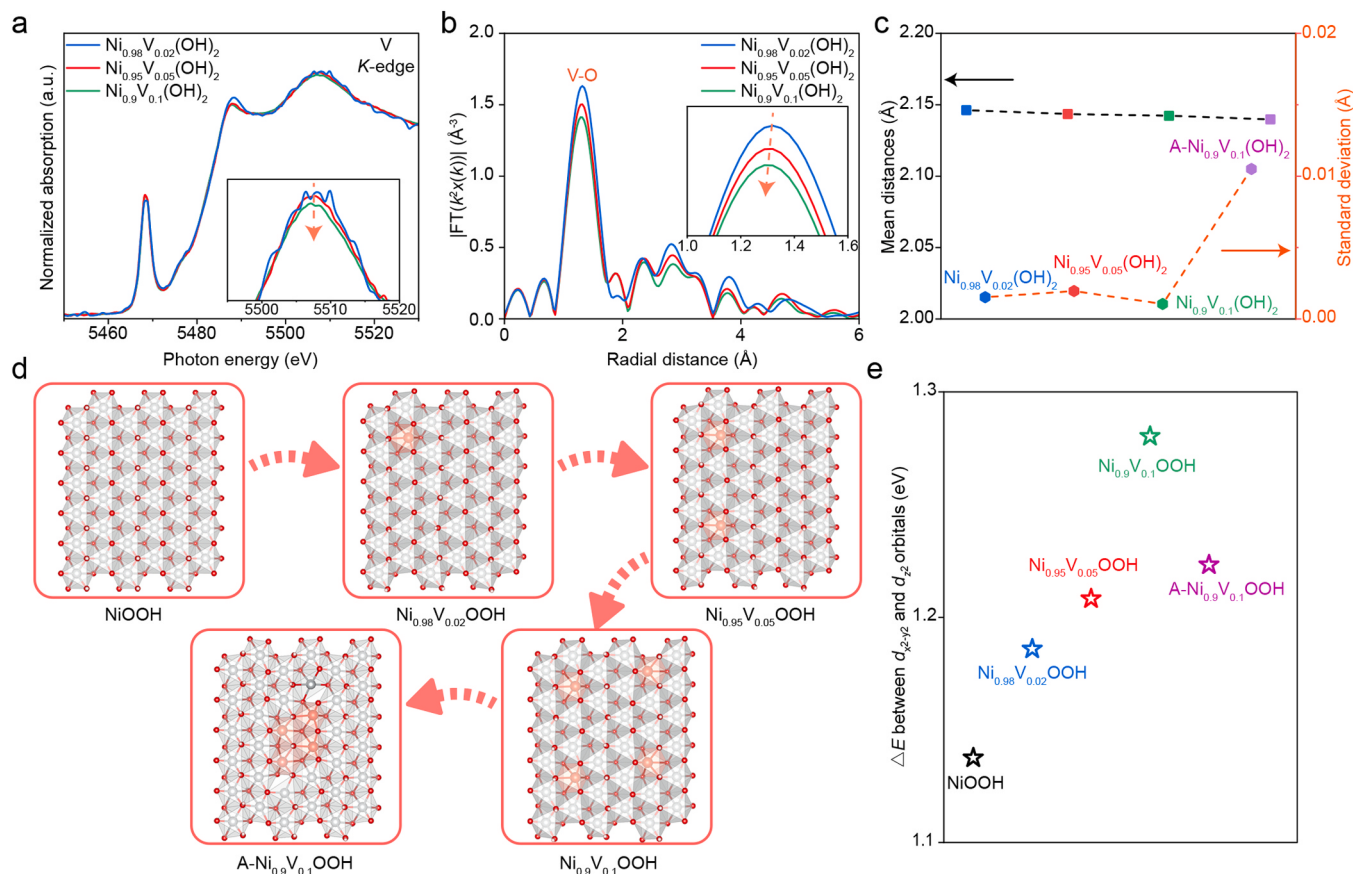


Fig. 2. Correlation of local V dopant environment with corresponding degree of NiO_6 octahedron distortion. a, Normalized V K-edge XAFS spectra of $\text{Ni}_{1-x}\text{V}_x(\text{OH})_2$ ($x = 0.02, 0.05, 0.10$). b, V K-edge FT-EXAFS spectra of $\text{Ni}_{1-x}\text{V}_x(\text{OH})_2$ ($x = 0.02, 0.05, 0.10$) (the inset shows the enlarged FT results within the range of 1.0 to 1.6 \AA). c, Mean distances and standard deviation of V-O bond lengths derived from the $\text{Ni}_{1-x}\text{V}_x(\text{OH})_2$ models in Fig. S8. d, Models of $\text{Ni}_{1-x}\text{V}_x\text{OOH}$ ($x \approx 0, 0.02, 0.05, 0.10$) with evenly distributed V and A- $\text{Ni}_{0.9}\text{V}_{0.1}\text{OOH}$ with aggregated V. e, Energy difference between $d_{x^2-y^2}$ and d_z^2 orbitals centers.

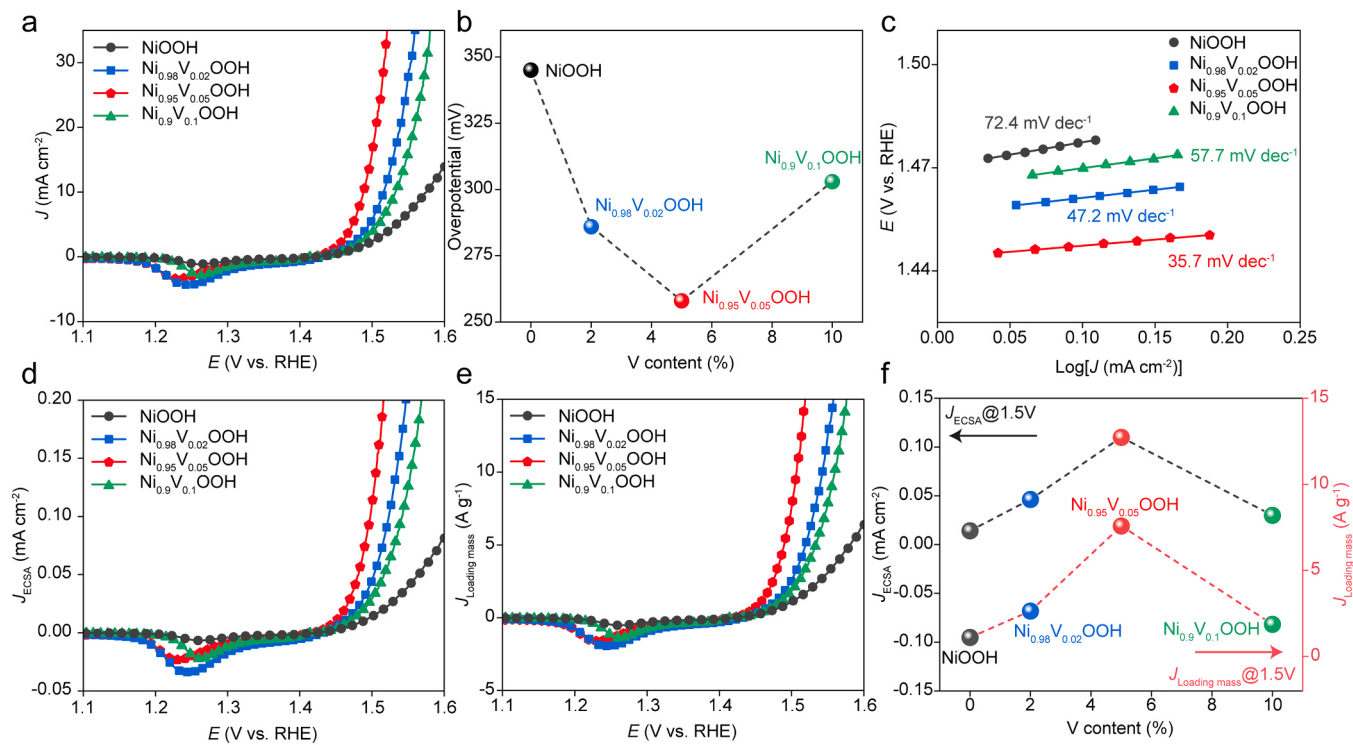


Fig. 3. Electrochemical oxygen evolution activities. a, Linear sweep voltammetry (LSV) curves of the $\text{Ni}_{1-x}\text{V}_x\text{OOH}$ ($x = 0, 0.02, 0.05, 0.10$) (iR -corrected). b, Overpotentials of the $\text{Ni}_{1-x}\text{V}_x\text{OOH}$ ($x = 0, 0.02, 0.05, 0.10$) at 10 mA cm^{-2} . c, Tafel plots of the $\text{Ni}_{1-x}\text{V}_x\text{OOH}$ ($x = 0, 0.02, 0.05, 0.10$). d, LSV curves of the $\text{Ni}_{1-x}\text{V}_x\text{OOH}$ ($x = 0, 0.02, 0.05, 0.10$) with current normalized to ECSA. e, LSV curves of the $\text{Ni}_{1-x}\text{V}_x\text{OOH}$ ($x = 0, 0.02, 0.05, 0.10$) with current normalized to loading mass, the loading masses of $\text{Ni}_{1-x}\text{V}_x\text{OOH}$ ($x = 0, 0.02, 0.05, 0.10$) is 2.18 mg cm^{-2} , 2.12 mg cm^{-2} , 2.23 mg cm^{-2} , 2.06 mg cm^{-2} , respectively. f, Comparison of the normalized current densities at 1.5 V versus RHE.

On the other hand, the FT-EXAFS spectra show that the V-O bond peak ($\sim 1.30 \text{ \AA}$) intensity follows the order: $\text{Ni}_{0.98}\text{V}_{0.02}(\text{OH})_2 > \text{Ni}_{0.95}\text{V}_{0.05}(\text{OH})_2 > \text{Ni}_{0.9}\text{V}_{0.1}(\text{OH})_2$. (Fig. 2b) In alignment with FT-EXAFS, the wavelet transform images of V K-edge display two maximum due to the V-O and V-Ni(V) contribution. Specifically, the wavelet transform plots show the gradually decreased intensity of V-O bond (around $k = 7 \text{ \AA}^{-1}$), further confirming the more distorted local environment of V with higher dopant concentration. (Fig. S9) This result further implies a more distorted V-O local environment with higher V dopant concentration, which is consistent with the V K-edge XAFS spectra analysis. Based on the detailed analysis of Ni K-edge and V K-edge XAFS spectra, it is hypothesized that the more irregular local V environment would represent a higher aggregation tendency in the $\text{Ni}(\text{OH})_2$ lattice. Specifically, when the dopant concentration is low, the V tend to be uniformly distributed in the host lattice, hence significantly perturbing the NiO_6 octahedron. In this regard, the V dopant would be surrounded by Ni elements. However, as the dopant concentration increases, the higher extent of aggregation of V would lead to weaker influence on the host lattice, hence the degree of NiO_6 distortion decreases. Meanwhile, the V would no longer be surrounded by Ni but the mix of V and Ni, thus resulting in a more irregular V-O local environment. To truly understand the influence of V dopant distribution situation on the V-O local environment, we build the $\text{Ni}_{1-x}\text{V}_x(\text{OH})_2$ models with different Ni:V ratios and different V cations distribution situations (Fig. S8). For those models with uniformly distributed V dopant, i.e., $\text{Ni}_{1-x}\text{V}_x(\text{OH})_2$ ($x \approx 0.02, 0.05, 0.10$), there is no V-O-V local environment observed in the lattice. As a result, the standard deviation of average V-O bond length does not show great difference. However, once there is V dopant aggregation in the host lattice, the appearance of V-O-V structure would lead to shorter V-O average bond distance compared to the uniformly distributed model (without V-O-V connections). (Fig. 2c, Fig. S8, Table S2) Moreover, the deviation of average V-O bond length increases dramatically with the

aggregation of V, indicating that the local V environment becomes more irregular. The decrease of average V-O bond length and more irregular local V environment due to V dopant aggregation well matches with the V K-edge EXAFS result. Therefore, the detailed XAFS analysis together with the density functional theory (DFT) calculation greatly validate the proposed hypothesis that V dopant would be more likely to aggregate in the lattice with higher concentration, leading to more disordered local V environment.

Given that the NiOOH is the real catalytic species under anodic potential, investigating the impact of the local environment of V dopant on the electronic states of NiOOH holds paramount significance. However, the Ni^{3+} is unstable and would be gradually reduced into Ni^{2+} via a self-discharge process, making it quite challenging to differentiate the structural difference among $\text{Ni}_{1-x}\text{V}_x\text{OOH}$ ($x = 0.02, 0.05, 0.1$) via XAFS technique [46]. Our previous work demonstrated that the conversion between $\text{Ni}(\text{OH})_2$ and NiOOH was a reversible process, hence the structural information of $\text{Ni}(\text{OH})_2$ could also reflect that of NiOOH [46]. Therefore, the degree of NiO_6 octahedron distortion of $\text{Ni}_{1-x}\text{V}_x\text{OOH}$ ($x = 0, 0.02, 0.05, 0.1$) should follow the same order as that of $\text{Ni}_{1-x}\text{V}_x(\text{OH})_2$ ($x = 0, 0.02, 0.05, 0.1$): $\text{Ni}_{0.95}\text{V}_{0.05}\text{OOH} > \text{Ni}_{0.98}\text{V}_{0.02}\text{OOH} > \text{Ni}_{0.9}\text{V}_{0.1}\text{OOH} > \text{NiOOH}$, showing a volcano-like relationship with the V dopant concentration. Here, the effect of local V environment on the NiO_6 octahedron distortion and the resultant electronic structure of NiOOH is further investigated through DFT calculations with the $\text{Ni}_{1-x}\text{V}_x\text{OOH}$ models derived from eliminating half of hydrogen atoms in the $\text{Ni}_{1-x}\text{V}_x(\text{OH})_2$ models. (Fig. 2d) Typically, the stronger NiO_6 octahedron distortion is positively related to the non-degenerate of $d_{x^2-y^2}$ and d_{z^2} orbitals with wider splitting energy gaps, showing higher extent of the e_g^* band broadening [17,31]. Here the orbital center difference between $d_{x^2-y^2}$ and d_{z^2} is used as a metric to quantify the extent of degeneracy of the e_g^* band [47]. As previously observed in Ni K-edge XAS spectra, the slightly reduced valence state in Ni^{2+} for $\text{Ni}(\text{OH})_2$ is

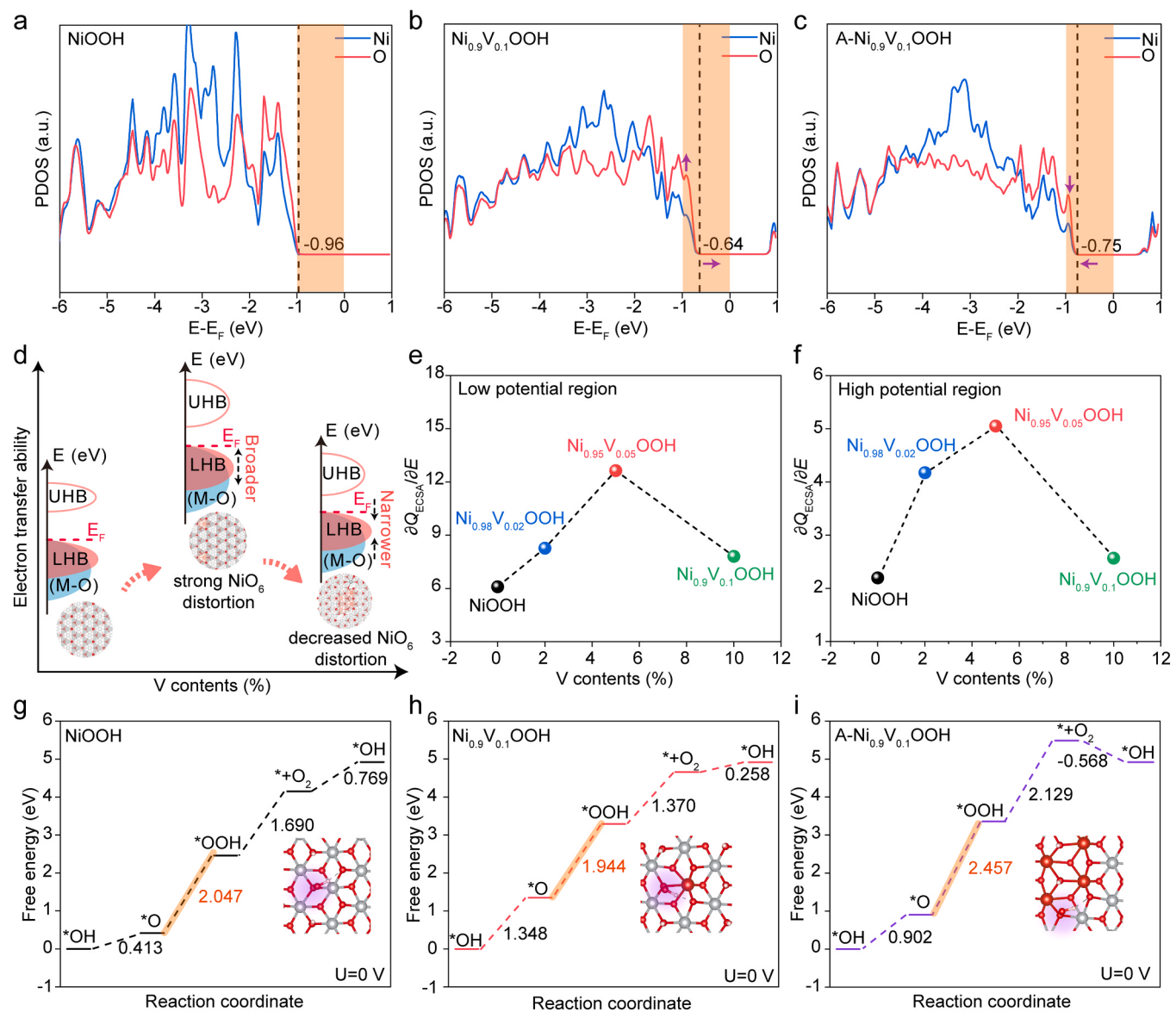


Fig. 4. Effect of V local environment on electron transfer ability. a, b, c, Projected density of states (PDOS) of NiOOH (a), Ni_{0.9}V_{0.1}OOH (b), and A-Ni_{0.9}V_{0.1}OOH (c). d, Schematic illustration of the influence of the local V environment on the broadening of the empty upper- and filled lower-Hubbard bands (denoted as UHB and LHB, respectively). e, f, Correlation between charge transfer ability and V content at low potential region (e) and high potential region (f). g, h, i, Free-energy diagrams for OER of NiOOH (g), Ni_{0.9}V_{0.1}OOH (h), and A-Ni_{0.9}V_{0.1}OOH (i).

associated with electron occupation in the e_g^* band, which would also contribute to the non-degenerate $d_{x^2-y^2}$ and d_{z^2} orbitals and hence the NiO₆ octahedron perturbation. (Fig. 1b) However, we find that there is negligible valence difference among Ni_{1-x}V_x(OH)₂ ($x = 0.02, 0.05, 0.10$) samples, which is also proved in the XPS results. (Fig. S10) Therefore, it could be inferred that the change in valence state of Ni after the incorporation of V dopant is not the dominant factor relating to the different extent of NiO₆ octahedron perturbation. As shown in Fig. 2e and Table S3, the orbital center difference between $d_{x^2-y^2}$ and d_{z^2} becomes progressively greater with higher uniformly distributed V dopant content, corresponding to higher extent of NiO₆ octahedron distortion. Upon the emergence of V-O-V connections within the NiOOH lattice (denoted as A-Ni_{0.9}V_{0.1}OOH), the capacity of V dopants to perturb the NiO₆ octahedron greatly diminishes. Consequently, a reduction in the splitting energy between $d_{x^2-y^2}$ and d_{z^2} can be observed in A-Ni_{0.9}V_{0.1}OOH. For the real situation, it should be noted that a larger scale of V dopants aggregation would occur than that in the A-Ni_{0.9}V_{0.1}OOH model, leading to further reduced extent of NiO₆

octahedron distortion. This is expected to result in a lower degree of NiO₆ octahedron distortion and narrower e_g^* band of Ni_{0.9}V_{0.1}OOH compared to Ni_{0.95}V_{0.05}OOH.

3.3. Comparison of intrinsic OER activities

In this section, the OER activities of Ni_{1-x}V_xOOH ($x = 0, 0.02, 0.05, 0.10$) samples are rigorously compared. It is worth mentioning that all electrocatalytic measurements are performed under Fe-removed 1 M KOH electrolyte to minimize the effect of Fe impurity on the measurement (detailed Fe impurity removal procedure is provided in the experimental section). The solution resistance (R_u) is used for iR -correction and its value is 2.57 Ω for Ni_{0.9}V_{0.1}OOH, 2.71 Ω for Ni_{0.95}V_{0.05}OOH, 2.80 Ω for Ni_{0.98}V_{0.02}OOH, and 2.85 Ω for NiOOH, respectively (Fig. S11). Fig. 3a shows the iR -corrected linear sweep voltammetry (LSV) curves of Ni_{1-x}V_xOOH ($x = 0, 0.02, 0.05, 0.10$) in 1 M KOH solution, with hydrothermal-electro oxidation derived NiOOH as benchmark. The downward peak observed from the gentle stage could

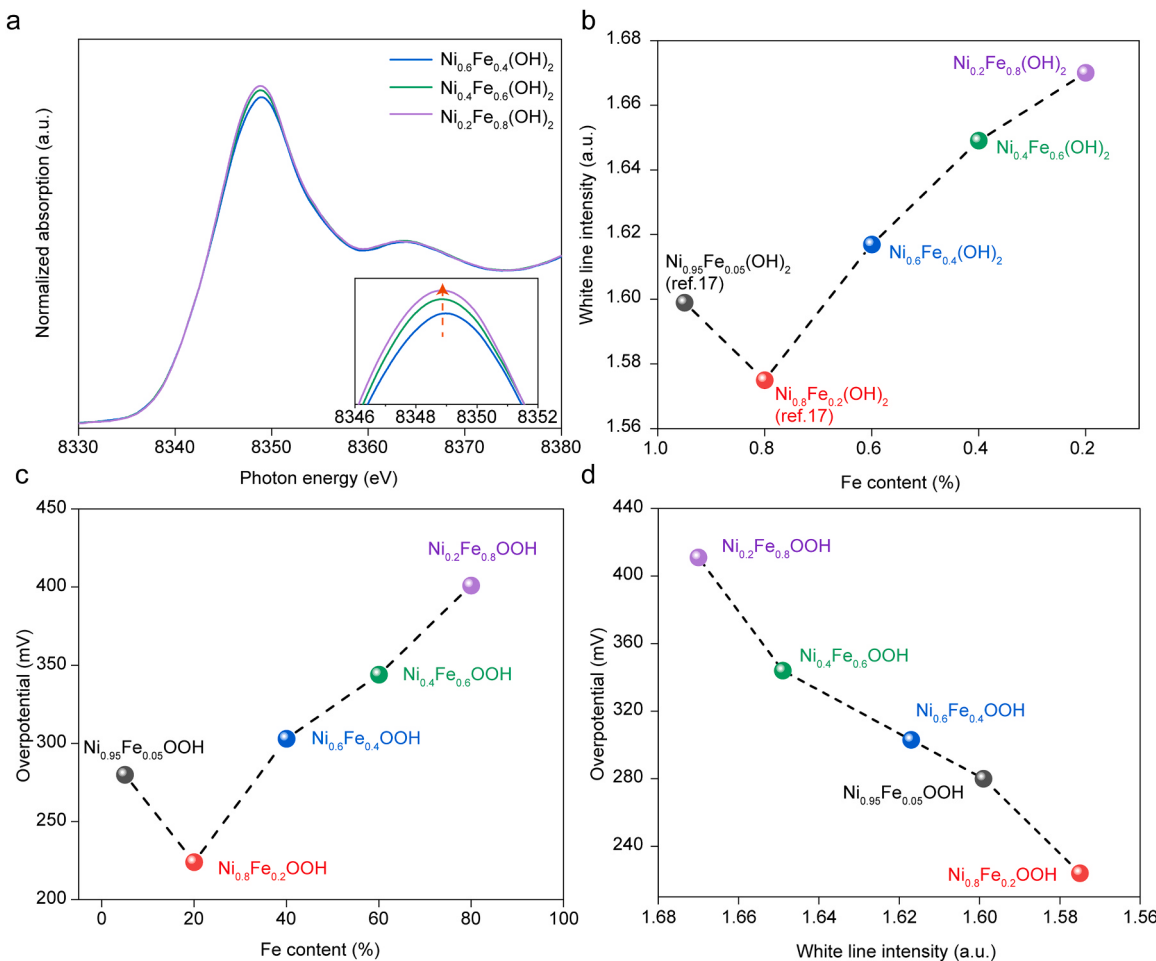


Fig. 5. Structural characterization and OER activities of NiFe system. a, Normalized Ni K-edge spectra of $\text{Ni}_{1-x}\text{Fe}_x(\text{OH})_2$ ($x = 0.4, 0.6, 0.8$). b, Normalized Ni K-edge white line intensity plots versus Fe contents, with the intensity of $\text{Ni}_{0.95}\text{Fe}_{0.05}(\text{OH})_2$ and $\text{Ni}_{0.8}\text{Fe}_{0.2}(\text{OH})_2$ extracted from Fig. 5a in our previous work [17]. c, LSV curves of $\text{Ni}_{1-x}\text{Fe}_x\text{OOH}$ ($x = 0.05, 0.2, 0.4, 0.6, 0.8$). d, Correlation between OER activity and NiO_6 octahedron perturbation in NiFe system. Here the white line intensity of $\text{Ni}_{1-x}\text{Fe}_x(\text{OH})_2$ is used to evaluate the NiO_6 octahedron perturbation for $\text{Ni}_{1-x}\text{Fe}_x\text{OOH}$ ($x = 0.05, 0.2, 0.4, 0.6, 0.8$) [17,33].

be attributed to the reduction from Ni^{3+} to Ni^{2+} due to the backward scan for the LSV measurement. It is revealed that the V-doped NiOOH samples with different dopants concentration exhibit various extent of OER activity improvement compared to the benchmark NiOOH . Specifically, $\text{Ni}_{0.98}\text{V}_{0.02}\text{OOH}$ exhibits a low overpotential of 286 mV at 10 mA cm^{-2} , which is 59 mV lower than that of benchmark NiOOH (overpotential of 345 mV at 10 mA cm^{-2}). With the V dopants content increases to $\sim 5\%$, the $\text{Ni}_{0.95}\text{V}_{0.05}\text{OOH}$ shows even better OER performance with overpotential of 258 mV at 10 mA cm^{-2} . However, further increases the V dopants concentration to $\sim 10\%$ would result in inferior OER activity, with overpotential of 303 mV at 10 mA cm^{-2} . (Fig. 3b) Fig. S12 provides the LSV curves of $\text{Ni}_{1-x}\text{V}_x\text{OOH}$ ($x = 0, 0.02, 0.05, 0.10$) without *iR*-correction, showing a consistent trend. Furthermore, the OER kinetics of $\text{Ni}_{1-x}\text{V}_x\text{OOH}$ ($x = 0, 0.02, 0.05, 0.10$) is evaluated by Tafel slope analysis, which is 72.4 mV dec^{-1} , 47.2 mV dec^{-1} , 35.7 mV dec^{-1} , 57.7 mV dec^{-1} for NiOOH , $\text{Ni}_{0.98}\text{V}_{0.02}\text{OOH}$, $\text{Ni}_{0.95}\text{V}_{0.05}\text{OOH}$, and $\text{Ni}_{0.9}\text{V}_{0.1}\text{OOH}$, respectively. (Fig. 3c) As such, the OER performance of $\text{Ni}_{1-x}\text{V}_x\text{OOH}$ ($x = 0, 0.02, 0.05, 0.10$) displays a volcano-like relationship with the V dopants content, reaching the highest around $\sim 5\%$ V. To compare the intrinsic activities of these samples, the current density is normalized to electrochemical surface area (ECSA) and loading mass. The normalized current density with respect to ECSA is presented in Fig. 3d, detailed information for the electrochemical double layer capacitance (C_{dl}) is provided in Fig. S13. The intrinsic OER performance is progressively improved with V dopants concentration increases to $\sim 5\%$, then decreased with the V content further reaches

$\sim 10\%$, exhibiting the highest intrinsic activity at around 5% V content. (Fig. 3d and f) Consistent results are also obtained when the current density is normalized to the loading mass (Fig. 3e and f). Thus, based on these results, the $\text{Ni}_{1-x}\text{V}_x\text{OOH}$ ($x = 0, 0.02, 0.05, 0.10$) samples possess different intrinsic OER activities, showcasing a pattern reminiscent of a volcano-like relationship with varying V dopants content.

3.4. Influence of local V environment on electron transfer ability

It is widely recognized that the electron transfer ability of OER electrocatalysts is closely linked to changes in the electronic states around the Fermi level [17,18,31]. To delve deeper into this relationship, we conduct DFT calculations to explore how the electronic states around the Fermi level would be affected by the local V environment. Here, three kinds of models i.e., NiOOH , $\text{Ni}_{0.9}\text{V}_{0.1}\text{OOH}$ with evenly distributed V, and A- $\text{Ni}_{0.9}\text{V}_{0.1}\text{OOH}$ with aggregated V are chosen to calculate the PDOS of the Ni and O orbitals. (Fig. 4a-c) In Fig. 4a, the Ni/O PDOS for pristine NiOOH shows a significantly small number of electronic states in the range from -1 to 0 eV , denoted by the orange shadow. When evenly distributed V cations are introduced into the NiOOH lattice, notable variations in the PDOS of both Ni and O orbitals become apparent. Specifically, the rising edge of the closest PDOS peak to the Fermi level is shifted from -0.96 to -0.64 eV . More importantly, there is a substantial increase in electronic states in the range from -1 to 0 eV for $\text{Ni}_{0.9}\text{V}_{0.1}\text{OOH}$ compared to that of NiOOH . (Fig. 4b) Conversely, when V aggregation occurs in the NiOOH structure, the

peak of PDOS near the Fermi level for both O and Ni becomes significantly lower and redshifted compared to $\text{Ni}_{0.9}\text{V}_{0.1}\text{OOH}$ with evenly distributed V (Fig. 4c). Combining these results with the understanding of the effects of local V dopant environment on the NiO_6 octahedron distortion, it becomes evident that the strong NiO_6 octahedron distortion induced by evenly distributed V dopants leads to a significant increase in the number of electronic states around the Fermi level. However, the aggregation of V dopants has a weaker influence on perturbing the NiO_6 octahedron, resulting in a narrower e_g^* band and, consequently, fewer electronic states around the Fermi level. (Fig. 4d) Theoretically, the higher number of electronic states near the Fermi level induced by stronger NiO_6 octahedron distortion would significantly enhance the electron transfer ability. To verify this, pulse-voltammetry measurements (Fig. S14) are carried out for $\text{Ni}_{1-x}\text{V}_x\text{OOH}$ ($x = 0, 0.02, 0.05, 0.10$), where the derived slope values from Fig. S15 could be used to describe the electron transfer rate from electrocatalysts to external circuit [48]. As shown in Fig. 4e and f, the electron transfer ability in both the low and high potential regions gradually strengthens as the amount of V increases from 0 to 5%. However, it weakens as the V concentration further increases to 10%, mirroring the variations in NiO_6 octahedron distortion degree. The higher electron transfer rate from electrocatalysts to external circuit caused by stronger NiO_6 octahedron distortion can lead to significantly improved OER activities. (Figs. S16-17) Furthermore, Gibbs free energy diagrams for OER of NiOOH , $\text{Ni}_{0.9}\text{V}_{0.1}\text{OOH}$, and $\text{A-Ni}_{0.9}\text{V}_{0.1}\text{OOH}$ are compared to study the influence of local V environment on the OER overpotentials. (Fig. 4g-i) It is revealed that the rate-determining step for all three models is the $^*\text{OOH}$ formation. The reaction free energy of $^*\text{OOH}$ formation for NiOOH is as high as 2.047 eV. After introducing evenly distributed V cations, the reaction free energy decreases to 1.944 eV, indicating an optimized OER pathway with a lower overpotential of 0.714 eV. In contrast, when V cations aggregate in the lattice, the adsorption Gibbs free energy of $^*\text{OOH}$ over the V-O-Ni site (denoted by the purple shadow in Fig. 4i) significantly increases, resulting in a much higher overpotential of 1.227 eV. These results show that the local V dopant environment plays a significant role in influencing the electronic states around the Fermi level and, consequently, OER activities.

3.5. Universal concept of local dopant environment on tuning NiO_6 octahedron perturbation in NiFe systems

We anticipate that this dependence of local dopant environment on tuning octahedron perturbation and corresponding OER activity is common. In support of this assertion, the correlation between the Fe dopant concentration and the degree of NiO_6 octahedron distortion is investigated in NiFe layered double hydroxides (LDH). Our previous work has revealed that with an increased amount of Fe dopant, the Ni K-edge white line intensity of $\text{Ni}_{1-x}\text{Fe}_x(\text{OH})_2$ ($x = 0.05, 0.20$) would be gradually reduced, indicating stronger NiO_6 octahedron distortion [17]. Here, the structural characteristics of $\text{Ni}_{1-x}\text{Fe}_x(\text{OH})_2$ ($x = 0.4, 0.6, 0.8$) are further studied via Ni K-edge XAFS spectra (Fig. 5c). It is revealed that further increase of Fe dopant content would lead to the narrower white line with higher intensities, indicating lower degree of NiO_6 octahedron distortion. Fig. 5b provides the correlation between the Fe dopant concentration and Ni K-edge white line intensity, where the data for $\text{Ni}_{0.95}\text{Fe}_{0.05}(\text{OH})_2$ and $\text{Ni}_{0.8}\text{Fe}_{0.2}(\text{OH})_2$ is extracted from Fig. 5a in our previous work [17]. Obviously, the degree of NiO_6 octahedron distortion in NiFe LDH system also exhibits a volcano-like relationship with the Fe dopant content, which is consistent with the phenomenon observed in the V-doped $\text{Ni}(\text{OH})_2$ system. Moreover, both the band center difference and the PDOS show that the evenly distributed Fe dopant leads to a higher number of electronic states around the Fermi level as well as the higher extent of e_g^* band broadening compared to the situation where Fe dopant is aggregated in lattice. (Figs. S18-19, Table. S4) The decreased ability on perturbing NiO_6 octahedron can be ascribed to the aggregation of Fe cations, forming Fe_2O_3 phase when its

content is higher than 20% [49]. (Fig. S20) Then, the OER activities of these NiFe LDH samples are investigated. (Fig. S21) The overpotential at 10 mA cm^{-2} is 280 mV, 224 mV, 303 mV, 344 mV, and 411 mV for $\text{Ni}_{0.95}\text{Fe}_{0.05}\text{OOH}$, $\text{Ni}_{0.8}\text{Fe}_{0.2}\text{OOH}$, $\text{Ni}_{0.6}\text{Fe}_{0.4}\text{OOH}$, $\text{Ni}_{0.4}\text{Fe}_{0.6}\text{OOH}$, and $\text{Ni}_{0.2}\text{Fe}_{0.8}\text{OOH}$, respectively, showing a volcano-like relationship with the Fe dopant concentration. (Fig. 5c) The distinct OER activity can be positively correlated with the degree of NiO_6 octahedron distortion, further proving the critical role of NiO_6 octahedron perturbation on optimizing the catalytic performance. (Fig. 5d) Therefore, these results corroborate the universality of this concept of local dopant environment on tuning NiO_6 octahedron perturbation and corresponding OER activities.

4. Conclusions

In summary, we demonstrate a novel understanding on the underlying mechanism of the widely observed volcano-like relationship between dopant concentration and OER activity in Ni-based oxyhydroxides by unraveling the effects of local V dopant environment on the NiO_6 octahedron perturbation. It turns out that uniformly distributed V dopant could induce strong NiO_6 octahedron distortion, resulting in strong e_g^* band broadening and highly efficient OER activity. However, higher content of the V dopant would be more likely to aggregate in the lattice, showing lower ability on perturbing the NiO_6 octahedron. In this regard, the extent of e_g^* band broadening would decrease, thus leading to lower number of electronic states around the Fermi level and inferior electron transfer ability from electrocatalysts to external circuit. As a result of balance between V doping and aggregation, the V-doped NiOOH reaches strongest NiO_6 octahedron distortion at around 5% V content, exhibiting superior OER activity with 258 mV at 10 mA cm^{-2} . In addition, we show the universality of this novel understanding by revealing the same effect in the NiFe LDH system. These findings would contribute to a deeper understanding of the structure-activity relationship in cation-doped materials and benefit for designing electrocatalysts with highly efficient activity.

CRediT authorship contribution statement

Yu Junchen: Conceptualization, Data curation, Formal analysis, Methodology, Validation, Visualization, Writing – original draft. **Zhong Haoyin:** Conceptualization, Data curation, Formal analysis, Methodology, Validation, Visualization, Writing – review & editing. **Zhang Qi:** Data curation, Formal analysis, Writing – review & editing. **Wu Chao:** Investigation. **Zhang Xin:** Investigation. **Li Shanlin:** Investigation. **Zhao Yongzhi:** Investigation. **An Hang:** Investigation. **Ma Yifan:** Investigation. **Yu Zhigen:** Investigation. **Xi Shibo:** Conceptualization, Supervision. **Wang Xiaopeng:** Conceptualization, Formal analysis, Writing – review & editing. **Xue Junmin:** Conceptualization, Project administration, Supervision, Writing – review & editing.

Declaration of Competing Interest

The authors declare that they have no known competing financial interests or personal relationships that could have appeared to influence the work reported in this paper.

Data availability

Data will be made available on request.

Acknowledgements

This research is supported by the National Research Foundation, Singapore, under its Competitive Research Programme (Award No.: NRF-CRP26-2021-0003) and Ministry of Education, Singapore, under its Academic Research Fund (AcRF) Tier 2 (Award No: MOE-

T2EP501220010). Agency for Science, Technology and Research (A*STAR) of Singapore. A*STAR, Grant No. of 152-70-00017.

Appendix A. Supporting information

The Supporting Information is available. Supporting Fig. S1–S21 and Supporting Tables S1–S4; additional characterizations of samples and electrochemical measurements; atomic models for DFT calculations. Supplementary data associated with this article can be found in the online version at doi:10.1016/j.apcatb.2023.123674.

References

- [1] F. Song, L. Bai, A. Moysiadou, S. Lee, C. Hu, L. Liardet, X. Hu, Transition metal oxides as electrocatalysts for the oxygen evolution reaction in alkaline solutions: an application-inspired renaissance, *J. Am. Chem. Soc.* 140 (2018) 7748–7759, <https://doi.org/10.1021/jacs.8b04546>.
- [2] L. Peng, N. Yang, Y. Yang, Q. Wang, X. Xie, D. Sun-Waterhouse, L. Shang, T. Zhang, G.I.N. Waterhouse, Atomic cation-vacancy engineering of NiFe-layered double hydroxides for improved activity and stability towards the oxygen evolution reaction, *Angew. Chem. Int. Ed.* 60 (2021) 24612–24619, <https://doi.org/10.1002/anie.202109938>.
- [3] J. Wang, Y. Gao, H. Kong, J. Kim, S. Choi, F. Ciucci, Y. Hao, S. Yang, Z. Shao, J. Lim, Non-precious-metal catalysts for alkaline water electrolysis: operando characterizations, theoretical calculations, and recent advances, *Chem. Soc. Rev.* 49 (2020) 9154–9196, <https://doi.org/10.1039/d0cs00575d>.
- [4] T. Wang, L. Tao, X. Zhu, C. Chen, W. Chen, S. Du, Y. Zhou, B. Zhou, D. Wang, C. Xie, P. Long, W. Li, Y. Wang, R. Chen, Y. Zou, X.-Z. Fu, Y. Li, X. Duan, S. Wang, Combined anodic and cathodic hydrogen production from aldehyde oxidation and hydrogen evolution reaction, *Nat. Catal.* 5 (2022) 66–73, <https://doi.org/10.1038/s41929-021-00721-y>.
- [5] F. Song, X. Hu, Exfoliation of layered double hydroxides for enhanced oxygen evolution catalysis, *Nat. Commun.* 5 (2014) 4477, <https://doi.org/10.1038/ncomms5477>.
- [6] Z.-Y. Yu, Y. Duan, X.-Y. Feng, X. Yu, M.-R. Gao, S.-H. Yu, Clean and affordable hydrogen fuel from alkaline water splitting: past, recent progress, and future prospects, *Adv. Mater.* 33 (2021) 2007100, <https://doi.org/10.1002/adma.202007100>.
- [7] W.M. Tong, M. Forster, F. Dionigi, S. Dresp, R.S. Erami, P. Strasser, A.J. Cowan, P. Farris, Electrolysis of low-grade and saline surface water, *Nat. Energy* 5 (2020) 367–377, <https://doi.org/10.1038/s41560-020-0550-8>.
- [8] J. Song, C. Wei, Z.-F. Huang, C. Liu, L. Zeng, X. Wang, Z.J. Xu, A review on fundamentals for designing oxygen evolution electrocatalysts, *Chem. Soc. Rev.* 49 (2020) 2196–2214, <https://doi.org/10.1039/C9CS00607A>.
- [9] N.-T. Suen, S.-F. Hung, Q. Quan, N. Zhang, Y.-J. Xu, H.M. Chen, Electrocatalysis for the oxygen evolution reaction: recent development and future perspectives, *Chem. Soc. Rev.* 46 (2017) 337–365, <https://doi.org/10.1039/C6CS00328A>.
- [10] J. Jiang, A. Zhang, L. Li, L. Ai, Nickel–cobalt layered double hydroxide nanosheets as high-performance electrocatalyst for oxygen evolution reaction, *J. Power Sources* 278 (2015) 445–451, <https://doi.org/10.1016/j.jpowsour.2014.12.085>.
- [11] T.X. Nguyen, Y.-C. Liao, C.-C. Lin, Y.-H. Su, J.-M. Ting, Advanced high entropy perovskite oxide electrocatalyst for oxygen evolution reaction, *Adv. Funct. Mater.* 31 (2021) 2101632, <https://doi.org/10.1002/adfm.202101632>.
- [12] M.S. Burke, M.G. Kast, L. Trotochaud, A.M. Smith, S.W. Boettcher, Cobalt–iron (oxy)hydroxide oxygen evolution electrocatalysts: the role of structure and composition on activity, stability, and mechanism, *J. Am. Chem. Soc.* 137 (2015) 3638–3648, <https://doi.org/10.1021/jacs.5b00281>.
- [13] A. Sumboja, J. Chen, Y. Zong, P.S. Lee, Z. Liu, NiMn layered double hydroxides as efficient electrocatalysts for the oxygen evolution reaction and their application in rechargeable Zn–air batteries, *Nanoscale* 9 (2017) 774–780, <https://doi.org/10.1039/C6NR08870H>.
- [14] X. Wang, H. Zhong, S. Xi, W.S.V. Lee, J. Xue, Understanding of Oxygen Redox in the Oxygen Evolution Reaction, *Adv. Mater.* 34 (2022) 2107956, <https://doi.org/10.1002/adma.202107956>.
- [15] Z.-F. Huang, J. Song, Y. Du, S. Xi, S. Dou, J.M.V. Nsanzimana, C. Wang, Z.J. Xu, X. Wang, Chemical and structural origin of lattice oxygen oxidation in Co–Zn oxyhydroxide oxygen evolution electrocatalysts, *Nat. Energy* 4 (2019) 329–338, <https://doi.org/10.1038/s41560-019-0355-9>.
- [16] S. Li, Z. Li, R. Ma, C. Gao, L. Liu, L. Hu, J. Zhu, T. Sun, Y. Tang, D. Liu, J. Wang, A glass-ceramic with accelerated surface reconstruction toward the efficient oxygen evolution reaction, *Angew. Chem. Int. Ed.* 60 (2021) 3773–3780, <https://doi.org/10.1002/anie.202014210>.
- [17] H. Zhong, X. Wang, G. Sun, Y. Tang, S. Tan, Q. He, J. Zhang, T. Xiong, C. Diao, Z. Yu, S. Xi, W.S.V. Lee, J. Xue, Optimization of oxygen evolution activity by tuning e^g band broadening in nickel oxyhydroxide, *Energy Environ. Sci.* 16 (2023) 641–652, <https://doi.org/10.1039/D2EE03413A>.
- [18] H. Zhong, Q. Zhang, J. Yu, X. Zhang, C. Wu, Y. Ma, H. An, H. Wang, J. Zhang, X. Wang, J. Xue, Fundamental understanding of structural reconstruction behaviors in oxygen evolution reaction electrocatalysts, *Adv. Energy Mater.* 13 (2023) 2301391, <https://doi.org/10.1002/aenm.202301391>.
- [19] P.M. Bodhankar, P.B. Sarawade, G. Singh, A. Vinu, D.S. Dhawale, Recent advances in highly active nanostructured NiFe LDH catalyst for electrochemical water splitting, *J. Mater. Chem. A* 9 (2021) 3180–3208, <https://doi.org/10.1039/DOTA10712C>.
- [20] S. Yu, Z. Xie, K. Li, L. Ding, W. Wang, G. Yang, F.-Y. Zhang, Morphology engineering of iridium electrodes via modifying titanium substrates with controllable pillar structures for highly efficient oxygen evolution reaction, *Electrochim. Acta* 405 (2022) 139797, <https://doi.org/10.1016/j.electacta.2021.139797>.
- [21] H.-F. Wang, C. Tang, B.-Q. Li, Q. Zhang, A review of anion-regulated multi-anion transition metal compounds for oxygen evolution electrocatalysis, *Inorg. Chem. Front.* 5 (2018) 521–534, <https://doi.org/10.1039/C7QI00780A>.
- [22] T. Zhao, X. Shen, Y. Wang, R.K. Hocking, Y. Li, C. Rong, K. Dastaftkan, Z. Su, C. Zhao, In situ reconstruction of V-doped Ni2P pre-catalysts with tunable electronic structures for water oxidation, *Adv. Funct. Mater.* 31 (2021) 2100614, <https://doi.org/10.1002/adfm.202100614>.
- [23] B. Wang, C. Tang, H.-F. Wang, X. Chen, R. Cao, Q. Zhang, A nanosized CoNi Hydroxide@Hydroxysulfide core-shell heterostructure for enhanced oxygen evolution, *Adv. Mater.* 31 (2019) 1805658, <https://doi.org/10.1002/adma.201805658>.
- [24] F.-Y. Chen, Z.-Y. Wu, Z. Adler, H. Wang, Stability challenges of electrocatalytic oxygen evolution reaction: from mechanistic understanding to reactor design, *Joule* 5 (2021) 1704–1731, <https://doi.org/10.1016/j.joule.2021.05.005>.
- [25] J. Kang, X. Qiu, Q. Hu, J. Zhong, X. Gao, R. Huang, C. Wan, L.-M. Liu, X. Duan, L. Guo, Valence oscillation and dynamic active sites in monolayer NiCo hydroxides for water oxidation, *Nat. Catal.* 4 (2021) 1050–1058, <https://doi.org/10.1038/s41929-021-00715-w>.
- [26] H. Li, P. Wen, Q. Li, C. Dun, J. Xing, C. Lu, S. Adhikari, L. Jiang, D.L. Carroll, S. M. Geyer, Retracted: earth-abundant iron diboride (FeB₂) nanoparticles as highly active bifunctional electrocatalysts for overall water splitting, *Adv. Energy Mater.* 7 (2017) 1700513, <https://doi.org/10.1002/aenm.201700513>.
- [27] Q. Wen, K. Yang, D. Huang, G. Cheng, X. Ai, Y. Liu, J. Fang, H. Li, L. Yu, T. Zhai, Schottky heterojunction nanosheet array achieving high-current-density oxygen evolution for industrial water splitting electrolyzers, *Adv. Energy Mater.* 11 (2021) 2102353, <https://doi.org/10.1002/aenm.202102353>.
- [28] J.R. Petrie, V.R. Cooper, J.W. Freeland, T.L. Meyer, Z. Zhang, D.A. Lutterman, H. N. Lee, Enhanced bifunctional oxygen catalysis in strained LaNiO₃ perovskites, *J. Am. Chem. Soc.* 138 (2016) 2488–2491, <https://doi.org/10.1021/jacs.5b11713>.
- [29] J. Bak, H.B. Bae, J. Kim, J. Oh, S.-Y. Chung, Formation of two-dimensional homologous faults and oxygen electrocatalytic activities in a perovskite nickelate, *Nano Lett.* 17 (2017) 3126–3132, <https://doi.org/10.1021/acs.nanolett.7b00561>.
- [30] R.D.L. Smith, C. Pasquini, S. Loos, P. Chernev, K. Klingan, P. Kubella, M. R. Mohammadi, D. González-Flores, H. Dau, Geometric distortions in nickel (oxy) hydroxide electrocatalysts by redox inactive iron ions, *Energy Environ. Sci.* 11 (2018) 2476–2485, <https://doi.org/10.1039/C8EE01063C>.
- [31] J. Bak, H. Bin Bae, S.-Y. Chung, Atomic-scale perturbation of oxygen octahedra via surface ion exchange in perovskite nickelates boosts water oxidation, *Nat. Commun.* 10 (2019) 2713, <https://doi.org/10.1038/s41467-019-10838-1>.
- [32] J. Bak, T.G. Yun, J.-S. An, H.B. Bae, S.-Y. Chung, Comparison of Fe-enhanced oxygen evolution electrocatalysis in amorphous and crystalline nickel oxides to evaluate the structural contribution, *Energy Environ. Sci.* 15 (2022) 610–620, <https://doi.org/10.1039/D1EE01826D>.
- [33] H. Zhong, Q. Zhang, J. Yu, X. Zhang, C. Wu, H. An, Y. Ma, H. Wang, J. Zhang, Y.-W. Zhang, C. Diao, Z.G. Yu, S. Xi, X. Wang, J. Xue, Key role of eg* band broadening in nickel-based oxyhydroxides on coupled oxygen evolution mechanism, *Nat. Commun.* 14 (2023) 7488, <https://doi.org/10.1038/s41467-023-43302-2>.
- [34] S. Klaus, M.W. Louie, L. Trotochaud, A.T. Bell, Role of catalyst preparation on the electrocatalytic activity of Ni1-xFexOOH for the oxygen evolution reaction, *J. Phys. Chem. C* 119 (2015) 18303–18316, <https://doi.org/10.1021/acs.jpcc.5b04776>.
- [35] R. Mahmood, W. Fan, X. Hu, J. Li, P. Liu, Y. Zhang, Z. Zhou, J. Wang, M. Liu, F. Zhang, Confirming high-valent iron as highly active species of water oxidation on the Fe, V-coupled bimetallic electrocatalyst: in situ analysis of X-ray absorption and Mössbauer spectroscopy, *J. Am. Chem. Soc.* (2023), <https://doi.org/10.1021/jacs.3c02288>.
- [36] K. Fan, H. Chen, Y. Ji, H. Huang, P.M. Claesson, Q. Daniel, B. Philippe, H. Rensmo, F. Li, Y. Luo, L. Sun, Nickel–vanadium monolayer double hydroxide for efficient electrochemical water oxidation, *Nat. Commun.* 7 (2016) 11981, <https://doi.org/10.1038/ncomms11981>.
- [37] J.M. Gonçalves, M. Irene da Silva, L. Angnes, K. Araki, Vanadium-containing electro and photocatalysts for the oxygen evolution reaction: a review, *J. Mater. Chem. A* 8 (2020) 2171–2206, <https://doi.org/10.1039/c9ta10857b>.
- [38] H.S. Chavan, C.H. Lee, A.I. Inamdar, J. Han, S. Park, S. Cho, N.K. Shreshta, S. U. Lee, B. Hou, H. Im, H. Kim, Designing and tuning the electronic structure of nickel–vanadium layered double hydroxides for highly efficient oxygen evolution electrocatalysis, *ACS Catal.* 12 (2022) 3821–3831, <https://doi.org/10.1021/acs.catal.1c05813>.
- [39] R. Mahmood, W. Fan, X. Hu, J. Li, P. Liu, Y. Zhang, Z. Zhou, J. Wang, M. Liu, F. Zhang, Confirming high-valent iron as highly active species of water oxidation on the Fe, V-coupled bimetallic electrocatalyst: in situ analysis of x-ray absorption and Mössbauer spectroscopy, *J. Am. Chem. Soc.* 145 (2023) 12206–12213, <https://doi.org/10.1021/jacs.3c02288>.
- [40] J.P. Perdew, K. Burke, M. Ernzerhof, Generalized Gradient Approximation Made Simple, *Phys. Rev. Lett.* 77 (1996) 3865–3868, <https://doi.org/10.1103/PhysRevLett.77.3865>.
- [41] S.L. Dudarev, G.A. Botton, S.Y. Savrasov, C.J. Humphreys, A.P. Sutton, Electron-energy-loss spectra and the structural stability of nickel oxide: An LSDA+U study, *Phys. Rev. B* 57 (1998) 1505–1509, <https://doi.org/10.1103/PhysRevB.57.1505>.

[42] G. Kresse, D. Joubert, From ultrasoft pseudopotentials to the projector augmented-wave method, Phys. Rev. B 59 (1999) 1758–1775, <https://doi.org/10.1103/PhysRevB.59.1758>.

[43] S. Grimme, S. Ehrlich, L. Goerigk, Effect of the damping function in dispersion corrected density functional theory, J. Comput. Chem. 32 (2011) 1456–1465, <https://doi.org/10.1002/jcc.21759>.

[44] V. Wang, N. Xu, J.-C. Liu, G. Tang, W.-T. Geng, VASPKIT: a user-friendly interface facilitating high-throughput computing and analysis using VASP code, Comput. Phys. Commun. 267 (2021) 108033, <https://doi.org/10.1016/j.cpc.2021.108033>.

[45] K. Momma, F. Izumi, VESTA 3 for three-dimensional visualization of crystal, volumetric and morphology data, J. Appl. Crystallogr. 44 (2011) 1272–1276, <https://doi.org/10.1107/S0021889811038970>.

[46] X.P. Wang, H.J. Wu, S.B. Xi, W.S.V. Lee, J. Zhang, Z.H. Wu, J.O. Wang, T.D. Hu, L. M. Liu, Y. Han, S.W. Chee, S.C. Ning, U. Mirsaidov, Z.B. Wang, Y.W. Zhang, A. Borgna, J. Wang, Y.H. Du, Z.G. Yu, S.J. Pennycook, J.M. Xue, Strain stabilized nickel hydroxide nanoribbons for efficient water splitting, Energy Environ. Sci. 13 (2020) 229–237, <https://doi.org/10.1039/C9EE02565K>.

[47] X. Wang, S. Xi, P. Huang, Y. Du, H. Zhong, Q. Wang, A. Borgna, Y.-W. Zhang, Z. Wang, H. Wang, Z.G. Yu, W.S.V. Lee, J. Xue, Pivotal role of reversible NiO₆ geometric conversion in oxygen evolution, Nature 611 (2022) 702–708, <https://doi.org/10.1038/s41586-022-05296-7>.

[48] H.N. Nong, L.J. Fallung, A. Bergmann, M. Klingenhof, H.P. Tran, C. Spöri, R. Mom, J. Timoshenko, G. Zichitella, A. Knop-Gericke, S. Piccinin, J. Pérez-Ramírez, B. R. Cuena, R. Schlögl, P. Strasser, D. Teschner, T.E. Jones, Key role of chemistry versus bias in electrocatalytic oxygen evolution, Nature 587 (2020) 408–413, <https://doi.org/10.1038/s41586-020-2908-2>.

[49] D. Friebel, M.W. Louie, M. Bajdich, K.E. Sanwald, Y. Cai, A.M. Wise, M.-J. Cheng, D. Sokaras, T.-C. Weng, R. Alonso-Mori, R.C. Davis, J.R. Bargar, J.K. Norskov, A. Nilsson, A.T. Bell, Identification of highly active Fe sites in (Ni,Fe)OOH for electrocatalytic water splitting, J. Am. Chem. Soc. 137 (2015) 1305–1313, <https://doi.org/10.1021/ja511559d>.